Anisotropy and redundancy governing undrained cyclic stress paths: closed-form modelling and micromechanical interpretation

Tokio Morimoto

Department of Civil Engineering, The University of Tokyo
7-3-1 Hongo, Bunkyo, Tokyo, 113-8656, Japan

Please note the manuscript has yet to be formally accepted for publication. Subsequent versions of this manuscript may have slightly different content. If accepted, the final version of this manuscript will be available via the 'Peer-reviewed Publication DOI' link on the right-hand side of this webpage.

Abstract

The undrained cyclic shear behaviour of sand leading to liquefaction cannot be predicted solely by traditional stress–dilatancy theories based on density and stress state; accounting for *fabric*, the microscopic structure of granular soils, is essential. This study develops a closed-form micromechanical model predicting increments in shear stress and mean effective stress during undrained cyclic simple shear across varied densities, stress states, and pre-shear histories. Building on Effective Medium Theory (EMT), which analytically links grain-scale properties and fabric to macroscopic moduli, the formulation incorporates stiffness degradation due to non-affine particle relaxation and contraction induced by contact sliding. We demonstrate that three internal variables—quantifying stiffness-weighted anisotropy, contact redundancy, and sliding-induced instability—govern the incremental shear modulus and dilatancy. Crucially, these variables are derived analytically from three quantities readily measurable in the Discrete Element Method (DEM): the contact normal fabric tensor, mechanical coordination number, and sliding contact fraction. Validated against DEM simulations across diverse packing states, the model provides a unified micromechanical interpretation of characteristic cyclic stress-path features, including phase transformation, pre-shear history effects, and anisotropic contraction.

Keywords: Anisotropy; discrete-element modelling; fabric/structure of soils; granular materials; liquefaction; stiffness.

1 Introduction

Liquefaction of sands, which has caused significant damage to infrastructure, is a consequence of progressive effective stress loss under undrained cyclic shear induced by earthquake ground motions (Ishihara, 1993). Predicting the undrained cyclic shear behaviour of sand remains challenging because the stress ratio evolves as the effective stress drops, decreases and increases in effective stress alternate, repeated load reversals occur, and sands at a similar density behave differently depending on their shear history. This complex behaviour stems from the nature of dilatancy, which is governed by factors such as stress state (Rowe, 1962), density (Been & Jefferies, 1985; Bolton, 1986), and soil microstructure (Li & Dafalias, 2012).

Figure 1(a) shows a typical stress path during undrained cyclic simple shear, obtained from Discrete Element Method (DEM) (Cundall & Strack, 1979) simulations by Morimoto & Salomon (2026), which is qualitatively consistent with cyclic torsional shear experiments on sand

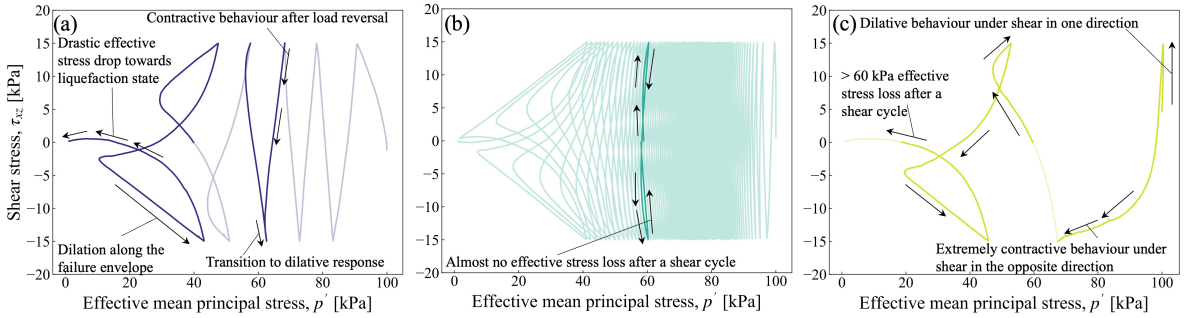


Figure 1: Undrained cyclic stress paths of three granular packings (Morimoto & Salomon, 2026) at similar void ratios e: (a) typical sample without cyclic pre-shear, (b) sample with a small cyclic pre-shear history, and (c) sample reconsolidated after liquefaction.

(Tatsuoka et al., 1986). Following a load reversal, the sample exhibits a decrease in effective mean principal stress p', hereafter termed *contraction* (with an increase in p' termed *dilation*), following standard liquefaction terminology (Ishihara, 1993) and analytical coupling relations (De Silva et al., 2015; Hu et al., 2020). Subsequently, the response transitions from contractive to dilative, known as *phase transformation* (Ishihara et al., 1975). As cyclic shearing progresses, dilation after phase transformation becomes more pronounced, followed by drastic contraction upon load reversal, eventually leading to liquefaction.

Previous experimental studies (Suzuki & Suzuki, 1988; Oda et al., 2001; Wahyudi et al., 2016) have shown that a small pre-shear history markedly increases liquefaction resistance. Consistently, a DEM sample with a similar void ratio to that in Figure 1(a) but subjected to a small cyclic pre-shear (Morimoto & Salomon, 2026) exhibits a much less contractive stress path (Figure 1(b)).

Conversely, a large pre-shear history such as prior liquefaction renders sand much more susceptible to liquefaction despite densification (Finn et al., 1970; Ishihara & Okada, 1978; Oda et al., 2001), a phenomenon known as *reliquefaction*. Figure 1(c) shows the stress path of the sample obtained by reconsolidating the liquefied sample in Figure 1(a), which exhibits substantially more contractive behaviour overall despite its lower void ratio. During the first cycle, the sample is initially stiff and dilative under shear in one direction ($\mathrm{d}\tau_{xz} > 0$), but contracts drastically after load reversal (Figure 1(c)). Such directional dependence is referred to as *anisotropic* behaviour (Oda, 1972; Arthur & Menzies, 1972; Miura & Toki, 1982), and laboratory studies (Ishihara & Okada, 1982; Yamada et al., 2010; Morimoto et al., 2019) have demonstrated that strong microstructural anisotropy develops following large pre-shearing such as liquefaction.

Because the samples in Figures 1(a)–(c) have nearly identical void ratios that remain constant throughout undrained shearing, accounting for the microscopic structure, or *fabric* (Oda, 1972), is essential to capture these distinct stress paths. Advanced constitutive models (e.g. Papadimitriou & Bouckovalas, 2002; Dafalias & Manzari, 2004; Zeng et al., 2026) have successfully reproduced cyclic liquefaction behaviour by incorporating fabric-related variables. Nevertheless, such continuum formulations rely on phenomenological coupling laws referenced to asymptotic states (e.g. the critical state or bounding/dilatancy surfaces) alongside history-dependent constructs such as memory surfaces and hardening parameters, whose particle-scale physical counterparts cannot be directly measured or uniquely identified from the instantaneous packing state. Consequently, a direct micromechanical link explaining how the current contact network alone governs the instantaneous stiffness and dilatancy remains elusive.

DEM provides a powerful means of directly accessing the particle-scale fabric of granular materials. Previous DEM studies on liquefaction and reliquefaction (Wang et al., 2016; Wei & Wang, 2017; Wang et al., 2019; Morimoto et al., 2021; Yang et al., 2022) have successfully

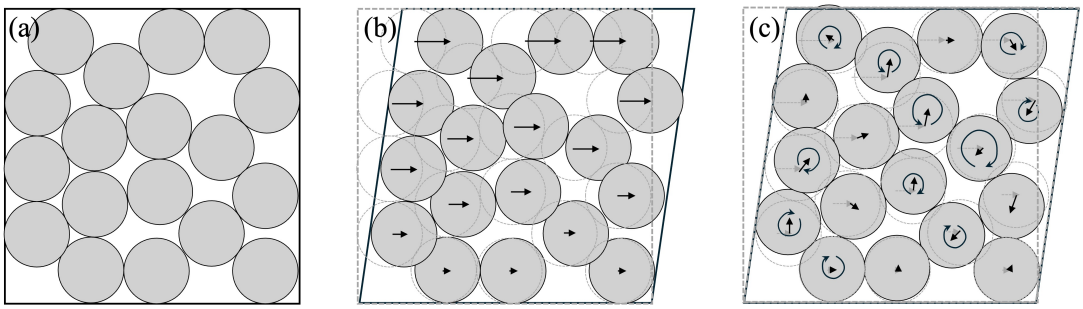


Figure 2: Schematic illustration of *affine* and *non-affine* kinematics in a granular packing: (a) initial configuration, (b) affine particle displacements complying with macroscopic deformation, and (c) additional non-affine translations and rotations relaxing unbalanced forces and torques.

distinguished samples at the same void ratio that exhibit contrasting cyclic shear responses using micromechanical variables, while tracking their evolution during shearing. Nevertheless, these studies have largely remained phenomenological, establishing empirical correlations between microscopic descriptors and macroscopic liquefaction resistance rather than a mechanics-based formulation that directly links the instantaneous fabric state to stiffness and dilatancy.

Effective Medium Theory (EMT) (Walton, 1987; Chang et al., 1989; Yimsiri & Soga, 2000) analytically links measurable micromechanical variables to the macroscopic moduli of a granular assembly by representing particles as nodes connected by contact springs. Under a prescribed macroscopic strain increment, classical EMT assumes that particle centres translate uniformly with the macroscopic strain field (*affine* displacement; Figures 2(a) and (b)), allowing contact deformations and macroscopic moduli to be evaluated analytically. In disordered packings, however, affine displacements generate unbalanced forces and torques on particles, inducing additional translations and rotations to restore equilibrium (*non-affine* motion; Figure 2(c)). Because classical EMT neglects this non-affine relaxation, it substantially overpredicts the moduli (Makse et al., 1999; Magnanimo et al., 2008; La Ragione & Magnanimo, 2012).

Non-affine corrections to EMT have been derived analytically for frictionless, isotropic spheres by Lemaître & Maloney (2006) and Zaccone & Scossa-Romano (2011), and extended semi-analytically to frictional, anisotropic spheres by Morimoto (2027) in the regime where contact sliding is negligible. Yet, undrained cyclic shear involves extensive contact sliding and irreversible rearrangement; accounting for finite inter-particle friction with sliding contacts is therefore essential to capture general cyclic stress–dilatancy behaviour.

This study develops closed-form expressions for the shear modulus and volumetric–shear coupling during undrained cyclic simple shear, informed by constant-volume DEM simulations across diverse densities and pre-shear histories. Extending the frameworks of Zaccone & Scossa-Romano (2011) and Morimoto (2027) beyond the non-sliding regime, we demonstrate that system anisotropy and mechanical redundancy govern the incremental stiffness and dilatancy, and that the controlling internal variables can be derived analytically from three standard DEM quantities: the contact normal fabric tensor, mechanical coordination number, and sliding contact fraction. The resulting model accurately predicts shear and effective stress increments at arbitrary points along cyclic stress paths, providing a unified micromechanical interpretation of key stress-path features such as those highlighted in Figure 1.

2 Methodology

2.1 Discrete Element Method (DEM)

A series of DEM simulations was conducted using the open-source code LAMMPS (Plimpton, 1995; Thompson et al., 2022). Spherical particles were employed because their undrained cyclic

stress paths (Figure 1) reproduce the essential qualitative features observed in natural sands. To capture the pressure dependency of soil stiffness (Hardin & Richart, 1963; Goddard, 1990; Yimsiri & Soga, 2000), a simplified Hertz–Mindlin contact model (Hertz, 1882; Mindlin, 1949; Mindlin & Deresiewicz, 1953), similar to that of Tsuji et al. (1992), was adopted. First, the elastic constants K_n and K_t (in Pa) are defined from the particle shear modulus G_p and Poisson's ratio ν_p as

$$K_\mathrm{n} = \frac{4G_\mathrm{p}}{3(1-\nu_\mathrm{p})}, \quad K_\mathrm{t} = \frac{4G_\mathrm{p}}{2-\nu_\mathrm{p}}. \tag{1}$$

The normal contact force vector $\mathbf{F}_\mathrm{n}$ is related to the particle overlap δ and unit contact normal $\mathbf{n}$ by

$$\mathbf{F}_\mathrm{n} = K_\mathrm{n}\delta^{\frac{3}{2}}\sqrt{R^*}\mathbf{n}, \tag{2}$$

where $R^* = R_1R_2/(R_1+R_2)$ is the equivalent radius of the two contacting particles with radii R_1 and R_2. The tangential contact force $\mathbf{F}_\mathrm{t}$ is computed incrementally from the relative tangential displacement increment $\Delta\mathbf{s}_\mathrm{t}$ as

$$\Delta\mathbf{F}_\mathrm{t} = -K_\mathrm{t}\sqrt{\delta R^*}\Delta\mathbf{s}_\mathrm{t}, \tag{3}$$

and updated subject to the Coulomb friction limit with inter-particle friction coefficient μ:

$$\mathbf{F}_\mathrm{t} = \min\left(\|\mathbf{F}_\mathrm{t}+\Delta\mathbf{F}_\mathrm{t}\|, \mu\|\mathbf{F}_\mathrm{n}\|\right)\frac{\mathbf{F}_\mathrm{t}+\Delta\mathbf{F}_\mathrm{t}}{\|\mathbf{F}_\mathrm{t}+\Delta\mathbf{F}_\mathrm{t}\|}. \tag{4}$$

2.2 Material properties

Nearly monodisperse spheres with a coefficient of uniformity of 1.1, median particle diameter $D_{50} = 8$ mm, and particle density $\rho_\mathrm{p} = 2600$ kg/m^3 were used. Based on grain-scale experiments on glass beads and quartz sand particles (Cavarretta, 2009; Senetakis et al., 2013), G_p and ν_p were set to 32 GPa and 0.22, respectively. An inter-particle friction coefficient of $\mu = 0.30$ was adopted as the baseline material property throughout the simulations unless stated otherwise.

3 Simulation procedures

3.1 Sample generation and isotropic compression

The sample preparation procedures follow Morimoto & Salomon (2026). A total of 7375 particles were randomly generated at an initial void ratio of 2.0 within a cubic domain bounded by periodic boundaries in all three directions. Each assembly was isotropically compressed to $p' = 100$ kPa using $\mu = 0.01$, 0.024, 0.06, 0.15, or 0.30 to obtain five isotropic samples with void ratios ranging from 0.5467 to 0.7109, denoted as IC-1 to IC-5, respectively.

3.2 Triaxial pre-shear

Isotropically compressed packings lack the inherent anisotropy typical of natural deposits or air-pluviated laboratory specimens. Following Yimsiri & Soga (2010) and Wei & Wang (2017), a drained triaxial pre-shear was applied with $\mu = 0.30$ to induce realistic initial anisotropy. Specifically, samples IC-2 and IC-3 were compressed in the vertical (z) direction at a constant lateral stress of 100 kPa up to axial strains of 0.8% and 1.2%, respectively, and then unloaded in drained triaxial extension at the same lateral stress until the axial stress returned to 100 kPa. This procedure yields an isotropic stress state ($p' = 100$ kPa) while retaining an anisotropic microstructure; the resulting dense and medium-dense parent samples are denoted as D-Initial and M-Initial, respectively.

3.3 Constant-volume cyclic pre-shear and reconsolidation

To reproduce the pre-shear history effects observed in laboratory tests, constant-volume cyclic simple shear, which is nearly equivalent to undrained cyclic simple shear (Monkul et al., 2015), was applied in the xz-plane to both D-Initial and M-Initial samples. Each sample was sheared at a constant strain rate of $\dot{\gamma}_{xz} = 0.01$ s^{-1} with a fixed sample height until the shear stress reached $\tau_{xz} = 10$ kPa, whereupon the loading direction was reversed ($\dot{\gamma}_{xz} = -0.01$ s^{-1}) until $\tau_{xz} = -10$ kPa. The inertial number I, defined as

$$I = \frac{|\dot{\gamma}_{xz}| D_{50}}{\sqrt{p'/\rho_{\mathrm{p}}}}, \tag{5}$$

was 1.3×10^{-4} even at $p' = 1$ kPa, confirming quasi-static conditions ($I < 1.0 \times 10^{-3}$; Da Cruz et al. 2005) throughout most of the simulation. During cyclic pre-shearing, p' gradually decreased while the double-amplitude shear strain increased. Pre-shearing was terminated at various stages, and each sample was isotropically reconsolidated to $p' = 100$ kPa, yielding 11 pre-sheared samples for each of the M- and D-series. Following Suzuki & Suzuki (1988) and Wahyudi et al. (2016), the maximum double-amplitude shear strain experienced during pre-shear, γ_{DAmax}, quantifies the pre-shear severity; for example, M-G1.03% denotes the sample reconsolidated after applying $\gamma_{\mathrm{DAmax}} = 1.03\%$ to M-Initial.

Table 1 summarises the initial states of all samples prior to the main cyclic shear. Whereas the conventional coordination number Z is defined from the total numbers of contacts N_{c} and particles N_{p} as

$$Z = \frac{2N_{\mathrm{c}}}{N_{\mathrm{p}}}, \tag{6}$$

the mechanical coordination number Z^* (Thornton, 2000) considers only mechanically active non-rattler particles (N_{p}^*, having at least two contacts) and their associated contacts (N_{c}^*):

$$Z^* = \frac{2N_{\mathrm{c}}^*}{N_{\mathrm{p}}^*}. \tag{7}$$

Similarly, the mechanical solid fraction ϕ^*, which provides a convenient density measure for EMT, is defined as

$$\phi^* = \frac{V_{\mathrm{s}}^*}{V}, \tag{8}$$

where V_{s}^* is the solid volume of non-rattler particles and V is the total sample volume. Finally, f_{xz} is the xz-component of the deviatoric contact normal fabric tensor f_{ij} (Ouadfel & Rothenburg, 2001):

$$f_{ij} = \frac{15}{2}\left(\phi_{ij} - \frac{1}{3}\mathrm{Tr}(\phi_{ij})\delta_{ij}\right), \tag{9}$$

where δ_{ij} is the Kronecker delta and ϕ_{ij} is the second-order contact normal fabric tensor (Satake, 1978; Oda, 1982),

$$\phi_{ij} = \frac{1}{N_{\mathrm{c}}}\sum_{c=1}^{N_{\mathrm{c}}} n_i^{(c)} n_j^{(c)}, \tag{10}$$

with $\mathbf{n}^{(c)}$ denoting the unit contact normal vector at contact c.

3.4 Main constant-volume cyclic shear

The 24 M- and D-series samples in Table 1 were then subjected to the main constant-volume cyclic simple shear following the same protocol as the pre-shear stage, except with a shear stress amplitude of ± 15 kPa. The number of cycles to initial liquefaction ($p' < 1$ kPa), N_{L}, is listed in Table 1. With increasing γ_{DAmax}, N_{L} initially increases markedly before dropping below

that of the non-presheared sample despite a lower void ratio (e.g. M-G5.33%), consistent with laboratory observations (Ishihara & Okada, 1978, 1982; Suzuki & Suzuki, 1988; Oda et al., 2001; Wahyudi et al., 2016).

At any point along a simulated cyclic path, the instantaneous stress state (p', τ_{xz}) and microscopic variables (e.g. Z^*, f_{xz}) can be extracted alongside the subsequent stress increments ($\mathrm{d}p'^{\mathrm{DEM}}$ and $\mathrm{d}\tau_{xz}^{\mathrm{DEM}}$) over a forward shear strain increment of $|\mathrm{d}\gamma_{xz}| = 1.0 \times 10^{-5}$. In what follows, samples M-Initial, M-G1.03% (high N_{L}), and M-G3.96% (low N_{L}), together with IC-1 to IC-5, are used for model formulation, while the remaining samples serve for validation.

Table 1: Summary of initial states (at $p' = 100$ kPa prior to main cyclic shear) and liquefaction resistances of the DEM samples.

Case	e	ϕ^*	Z^*	f_{xz}	γ_{DAmax}	N_{L}
IC-1	0.5467	0.634	6.14	0.010	—	—
IC-2	0.5858	0.614	5.84	−0.009	—	—
IC-3	0.6206	0.594	5.56	−0.022	—	—
IC-4	0.6678	0.564	5.15	−0.012	—	—
IC-5	0.7109	0.533	4.72	−0.022	—	—
M-Initial	0.6224	0.571	4.76	−0.014	0%	5.5
M-G0.03%	0.6219	0.571	4.87	−0.003	0.03%	8.5
M-G0.05%	0.6217	0.571	4.91	−0.016	0.05%	19.5
M-G0.1%	0.6213	0.571	4.94	0.042	0.1%	37.5
M-G0.4%	0.6212	0.571	4.95	−0.063	0.4%	25.5
M-G0.7%	0.6207	0.572	5.00	−0.066	0.7%	55.5
M-G1.03%	0.6203	0.572	5.00	0.007	1.03%	83.5
M-G1.57%	0.6197	0.572	4.93	−0.099	1.57%	6.5
M-G2.09%	0.6188	0.572	4.92	0.017	2.09%	14
M-G3%	0.6179	0.573	4.89	−0.107	3%	1.5
M-G3.96%	0.6163	0.573	4.86	0.064	3.96%	2
M-G5.33%	0.6137	0.574	4.86	−0.111	5.33%	0.5
D-Initial	0.5899	0.613	4.78	−0.016	0%	5.5
D-G0.04%	0.5891	0.613	4.91	−0.020	0.04%	10
D-G0.05%	0.5890	0.613	4.92	−0.020	0.05%	14.5
D-G0.1%	0.5887	0.613	4.96	−0.050	0.1%	35
D-G0.4%	0.5885	0.613	4.97	−0.064	0.4%	31.5
D-G0.7%	0.5880	0.613	5.05	0.004	0.7%	>1000
D-G1%	0.5878	0.613	5.04	−0.047	1%	187
D-G1.61%	0.5872	0.614	5.03	0.023	1.61%	103
D-G2.12%	0.5866	0.614	4.98	−0.071	2.12%	31
D-G3.05%	0.5857	0.614	4.94	0.065	3.05%	8.5
D-G4.07%	0.5845	0.615	4.90	−0.086	4.07%	2.5
D-G4.84%	0.5836	0.615	4.87	0.072	4.84%	2

4 Model formulation

4.1 Effective Medium Theory (EMT)

Under the affine kinematics assumption (Figure 2(b)), EMT relates the contact-scale microstructure of a granular packing directly to its macroscopic moduli (Walton, 1987; Chang et al., 1989). For the simplified Hertz–Mindlin model adopted here, the incremental normal and tangential

contact stiffnesses read

$$k_{\mathrm{n}} = \frac{\mathrm{d}F_{\mathrm{n}}}{\mathrm{d}\delta} = \frac{3}{2} K_{\mathrm{n}} \sqrt{R^*} \delta^{\frac{1}{2}}, \tag{11}$$

$$k_{\mathrm{t}} = \frac{\mathrm{d}\|\mathbf{F}_{\mathrm{t}}\|}{\mathrm{d}\|\Delta\mathbf{s}_{\mathrm{t}}\|} = K_{\mathrm{t}} \sqrt{R^*} \delta^{\frac{1}{2}}, \tag{12}$$

where $F_{\mathrm{n}} \equiv \|\mathbf{F}_{\mathrm{n}}\|$. Denoting the contact stiffness ratio by A, we have

$$A \equiv \frac{k_{\mathrm{n}}}{k_{\mathrm{t}}} = \frac{2 - \nu_{\mathrm{p}}}{2(1 - \nu_{\mathrm{p}})}. \tag{13}$$

Following Walton (1987) and Chang et al. (1989), Morimoto (2027) expressed the affine shear modulus $C_{xzxz} = \mathrm{d}\tau_{xz}/\mathrm{d}\gamma_{xz}$ in terms of k_{n} and A as

$$C_{xzxz}^{\mathrm{EMT}} = \frac{N_{\mathrm{c}}^*}{V} \frac{2A + 3}{30A} \langle L^2 k_{\mathrm{n}} \rangle, \tag{14}$$

where L is the branch length between the centres of contacting particles and $\langle \cdot \rangle$ denotes the arithmetic mean over mechanical contacts. Similarly, Morimoto (2027) defined the volumetric–shear coupling modulus as

$$\begin{aligned} C_{\mathrm{vol},xz} &\equiv C_{xxxz} + C_{yyxz} + C_{zzxz} \\ &= \frac{\mathrm{d}\sigma'_{xx} + \mathrm{d}\sigma'_{yy} + \mathrm{d}\sigma'_{zz}}{\mathrm{d}\gamma_{xz}} = \frac{3\,\mathrm{d}p'}{\mathrm{d}\gamma_{xz}}, \end{aligned} \tag{15}$$

and derived its EMT estimate as

$$C_{\mathrm{vol},xz}^{\mathrm{EMT}} = \frac{N_{\mathrm{c}}^*}{V} \langle L^2 k_{\mathrm{n}} n_x n_z \rangle. \tag{16}$$

Using the relationship between p' and the mean normal contact force (Rothenburg & Bathurst, 1989),

$$p' = \frac{1}{3} \frac{N_{\mathrm{c}}^*}{V} \langle L \rangle \langle F_{\mathrm{n}} \rangle, \tag{17}$$

and assuming monodispersity (Morimoto, 2027), the factor $\frac{N_{\mathrm{c}}^*}{V} \langle L^2 k_{\mathrm{n}} \rangle$ can be written in terms of p', the particle elastic constants $(\nu_{\mathrm{p}}, K_{\mathrm{n}})$, and the packing state (Z^*, ϕ^*) as

$$\frac{N_{\mathrm{c}}^*}{V} \langle L^2 k_{\mathrm{n}} \rangle = A \frac{9 \cdot 2^{1/3}}{2\pi^{2/3}} \frac{1 - \nu_{\mathrm{p}}}{2 - \nu_{\mathrm{p}}} K_{\mathrm{n}}^{2/3} p'^{1/3} (Z^* \phi^*)^{2/3}. \tag{18}$$

Introducing the dimensionless material constant

$$B \equiv \frac{9 \cdot 2^{1/3}}{2\pi^{2/3}} \frac{1 - \nu_{\mathrm{p}}}{2 - \nu_{\mathrm{p}}}, \tag{19}$$

the EMT estimates of C_{xzxz}^{EMT} and $C_{\mathrm{vol},xz}^{\mathrm{EMT}}$ simplify to

$$C_{xzxz}^{\mathrm{EMT}} = B \frac{2A + 3}{30} K_{\mathrm{n}}^{2/3} p'^{1/3} (Z^* \phi^*)^{2/3}, \tag{20}$$

$$C_{\mathrm{vol},xz}^{\mathrm{EMT}} = \alpha A B K_{\mathrm{n}}^{2/3} p'^{1/3} (Z^* \phi^*)^{2/3}, \tag{21}$$

where $\alpha \equiv \langle k_{\mathrm{n}} n_x n_z \rangle / \langle k_{\mathrm{n}} \rangle$ represents the stiffness-weighted contact normal anisotropy. Combining Hertzian contact mechanics (Hertz, 1882) with the stress–force–fabric (SFF) relationship (Rothenburg & Bathurst, 1989; Bathurst & Rothenburg, 1990), Morimoto (2027) analytically approximated α as

$$\alpha \approx \frac{2}{45} f_{xz} + \frac{1}{9} \frac{\tau_{xz}}{p'}. \tag{22}$$

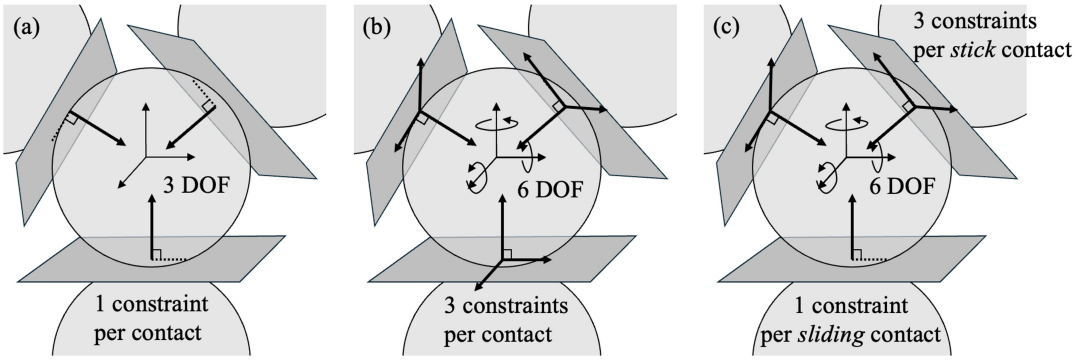


Figure 3: Degrees-of-freedom (DOF) analysis for (a) smooth spheres, (b) frictional spheres without contact sliding ($\mu \to \infty$), and (c) frictional spheres with finite μ, where both stick and sliding contacts coexist.

4.2 Non-affine correction without contact sliding

Although equations (20) and (21) contain no fitting parameters, they mispredict the actual moduli because affine displacements induce unbalanced forces and torques that are relaxed through non-affine particle motions (Figure 2(c); Makse et al. 1999).

For frictionless, isotropic spheres, Zaccone & Scossa-Romano (2011) analytically derived the effective shear modulus accounting for non-affine relaxation based on Lemaître & Maloney (2006)'s formalism:

$$C_{xzxz} = \frac{Z^* - Z^*_{\mathrm{crit}}}{Z^*} C^{\mathrm{EMT}}_{xzxz}, \tag{23}$$

where Z^*_{crit} is the critical mechanical coordination number. In a frictionless packing (Figure 3(a)), each sphere has three translational degrees of freedom (DOF) because zero tangential forces induce no particle rotation, while each contact provides one normal constraint. Mechanical stability requires $N^*_{\mathrm{c}} \geq 3N^*_{\mathrm{p}}$, giving $Z^*_{\mathrm{crit}} = 6$. Thus, C_{xzxz} vanishes at the mechanical stability limit $Z^* = Z^*_{\mathrm{crit}}$ (often termed the *isostatic limit*) and approaches C^{EMT}_{xzxz} as contact redundancy increases.

Natural sand, however, is frictional and typically anisotropic; rotation–translation coupling and fabric anisotropy preclude a purely analytical non-affine correction. Empirically, Morimoto (2027) demonstrated that in the regime where contact sliding is negligible, the effective shear modulus follows a similar attenuation form:

$$C_{xzxz} = \frac{Z^* - Z^*_{\mathrm{crit}}}{Z^* - Z^*_{\mathrm{crit}} + \lambda} C^{\mathrm{EMT}}_{xzxz}, \tag{24}$$

with $\lambda = 1.25$. When contact sliding is absent (equivalent to $\mu \to \infty$; Figure 3(b)), each sphere possesses six DOF (three translational and three rotational) and each contact supplies three constraints; stability requires $3N^*_{\mathrm{c}} \geq 6N^*_{\mathrm{p}}$, yielding $Z^*_{\mathrm{crit}} = 4$.

Whereas Zaccone & Scossa-Romano (2011) considered isotropic packings with $C_{\mathrm{vol},xz} = 0$, Morimoto (2027) evaluated the effective volumetric–shear coupling modulus in the non-sliding regime, denoted here as $C^{\alpha}_{\mathrm{vol},xz}$, using small-strain probes on the present DEM samples. As shown in Figure 4, $C^{\alpha}_{\mathrm{vol},xz}$ scales linearly with $C^{\mathrm{EMT}}_{\mathrm{vol},xz}$:

$$C^{\alpha}_{\mathrm{vol},xz} = k_{\mathrm{vol}} C^{\mathrm{EMT}}_{\mathrm{vol},xz}, \tag{25}$$

where $k_{\mathrm{vol}} = 1.5$ is an empirical constant (Morimoto, 2027).

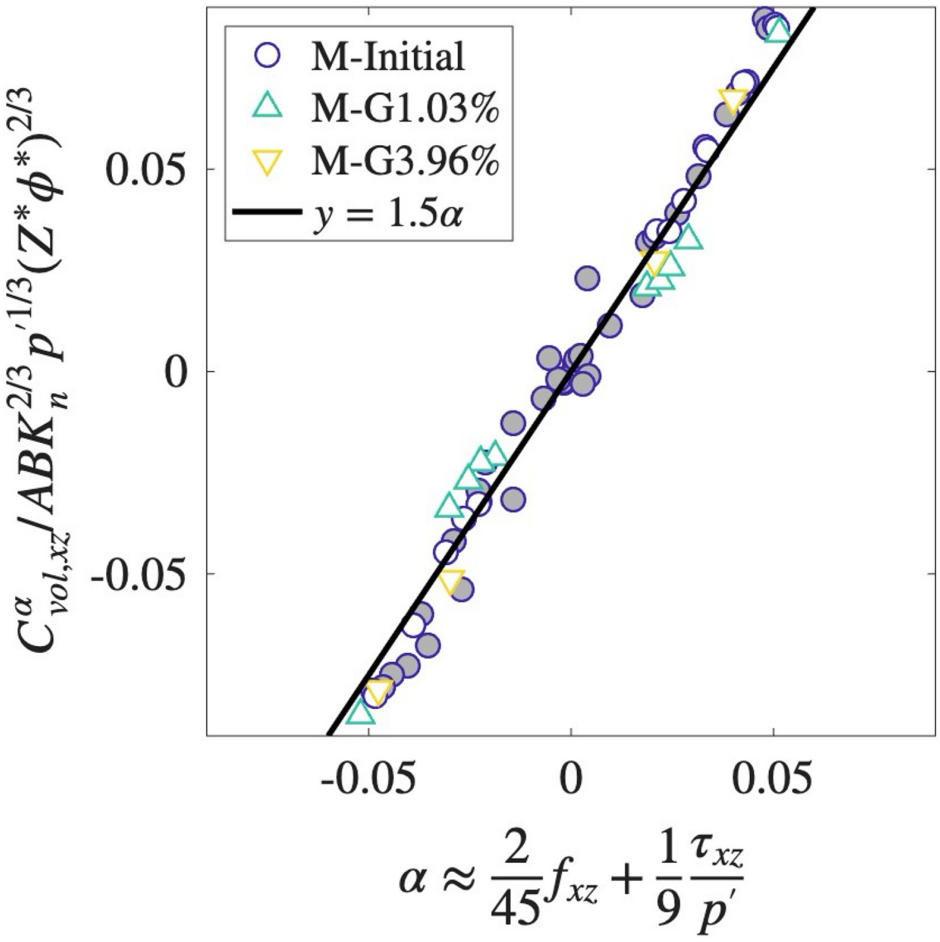


Figure 4: Normalised $C^{\alpha}_{\mathrm{vol},xz}$ versus α (Morimoto, 2027). Marker shapes denote sample cases, while coloured and grey fills indicate probe points at $|\tau_{xz}| = 15$ kPa and $|\tau_{xz}| < 15$ kPa, respectively.

4.3 System redundancy analysis considering sliding contacts

Because Morimoto (2027)'s model assumes negligible contact sliding, it cannot describe general undrained cyclic shear paths such as those in Figure 1: equation (24) fails to capture the rapid degradation of shear stiffness during shearing, while equation (25) predicts only minor dilatancy near $\tau_{xz} \approx 0$ kPa where substantial contraction actually occurs (Figure 1). For grains with a finite friction coefficient (Cavarretta, 2009; Senetakis et al., 2013), sticking and sliding contacts coexist during shearing. Because sliding contacts have reached the Coulomb friction limit, their incremental tangential stiffness vanishes. As illustrated in Figure 3(c), each sphere has six DOF, whereas sticking and sliding contacts provide three constraints and one normal constraint, respectively; mechanical stability therefore requires

$$3N_{\mathrm{c}}^{*\mathrm{stick}} + N_{\mathrm{c}}^{*\mathrm{sliding}} \geq 6N_{\mathrm{p}}^{*}. \tag{26}$$

Introducing the sliding contact fraction $f_{\mathrm{s}} \equiv N_{\mathrm{c}}^{*\mathrm{sliding}}/N_{\mathrm{c}}^{*}$, where $N_{\mathrm{c}}^{*\mathrm{sliding}}$ is the number of non-rattler contacts mobilising the Coulomb limit ($\|\mathbf{F}_{\mathrm{t}}\| = \mu\|\mathbf{F}_{\mathrm{n}}\|$), this stability condition can be rewritten as

$$Z^{*}(3 - 2f_{\mathrm{s}}) \geq 12. \tag{27}$$

4.4 Effect of contact sliding on shear modulus

Whereas Zaccone & Scossa-Romano (2011) and Morimoto (2027) scaled the affine shear modulus using Z^{*} and Z_{crit}^{*} (equations (23) and (24)), a natural extension to systems with sliding contacts is to adopt the redundancy index ρ (Kruyt & Rothenburg, 2009; Kruyt, 2010; Gong et al., 2012), defined from equation (27) as

$$\rho \equiv \frac{Z^{*}(3 - 2f_{\mathrm{s}})}{12} \geq 1. \tag{28}$$

To isolate the shear stiffness from the coupling effect of changing p' when back-calculating from DEM data, we use the total differential $\mathrm{d}\tau_{xz} = \eta\,\mathrm{d}p' + p'\,\mathrm{d}\eta$ (with $\eta \equiv \tau_{xz}/p'$) and define

$$C_{xzxz}^{\rho} \equiv \frac{\mathrm{d}\tau_{xz}^{\mathrm{DEM}} - \eta\,\mathrm{d}p'^{\mathrm{DEM}}}{\mathrm{d}\gamma_{xz}}, \tag{29}$$

denoting this net modulus by C_{xzxz}^{ρ} because it is governed by ρ. Following Zaccone & Scossa-Romano (2011) and Morimoto (2027), we write $C_{xzxz}^{\rho} = f(\rho)C_{xzxz}^{\mathrm{EMT}}$. Figure 5 plots $C_{xzxz}^{\rho}/C_{xzxz}^{\mathrm{EMT}}$ against ρ for the IC, M-Initial, M-G1.03%, and M-G3.96% samples (with the IC samples included to span a wider range of ρ and verify applicability to isotropic packings). The ratio $C_{xzxz}^{\rho}/C_{xzxz}^{\mathrm{EMT}}$ drops rapidly as ρ approaches the mechanical stability limit ($\rho = 1$). Most of the data follow an attenuation curve analogous to equation (24), $(\rho-\rho_1)/(\rho-\rho_1+c)$ with $\rho_1 = 1.033$ and $c = 0.283$ (consistent with $\lambda/4 = 0.313$ at $f_{\mathrm{s}} = 0$), while a small non-zero tail persists over $1 < \rho \leq \rho_2$ (inset of Figure 5). We therefore propose the piecewise function

$$f(\rho) = \begin{cases} 0 & (\rho \leq 1), \\ b(\rho - 1)^2 & (1 < \rho \leq \rho_2), \\ \dfrac{\rho - \rho_1}{\rho - \rho_1 + c} & (\rho > \rho_2), \end{cases} \tag{30}$$

where $b = 1/8$, $c = 0.283$, and $\rho_1 = 1.033$ are empirical constants, and $\rho_2 \approx 1.043$ is determined algebraically from the intersection of the two branches.

4.5 Effect of contact sliding on volumetric–shear coupling modulus

The contribution of contact sliding to the volumetric–shear coupling can be isolated by subtracting the non-sliding response from the DEM increment in p':

$$\mathrm{d}p'^{\mathrm{sliding}} = \mathrm{d}p'^{\mathrm{DEM}} - \frac{C_{\mathrm{vol},xz}^{\alpha}\mathrm{d}\gamma_{xz}}{3}. \tag{31}$$

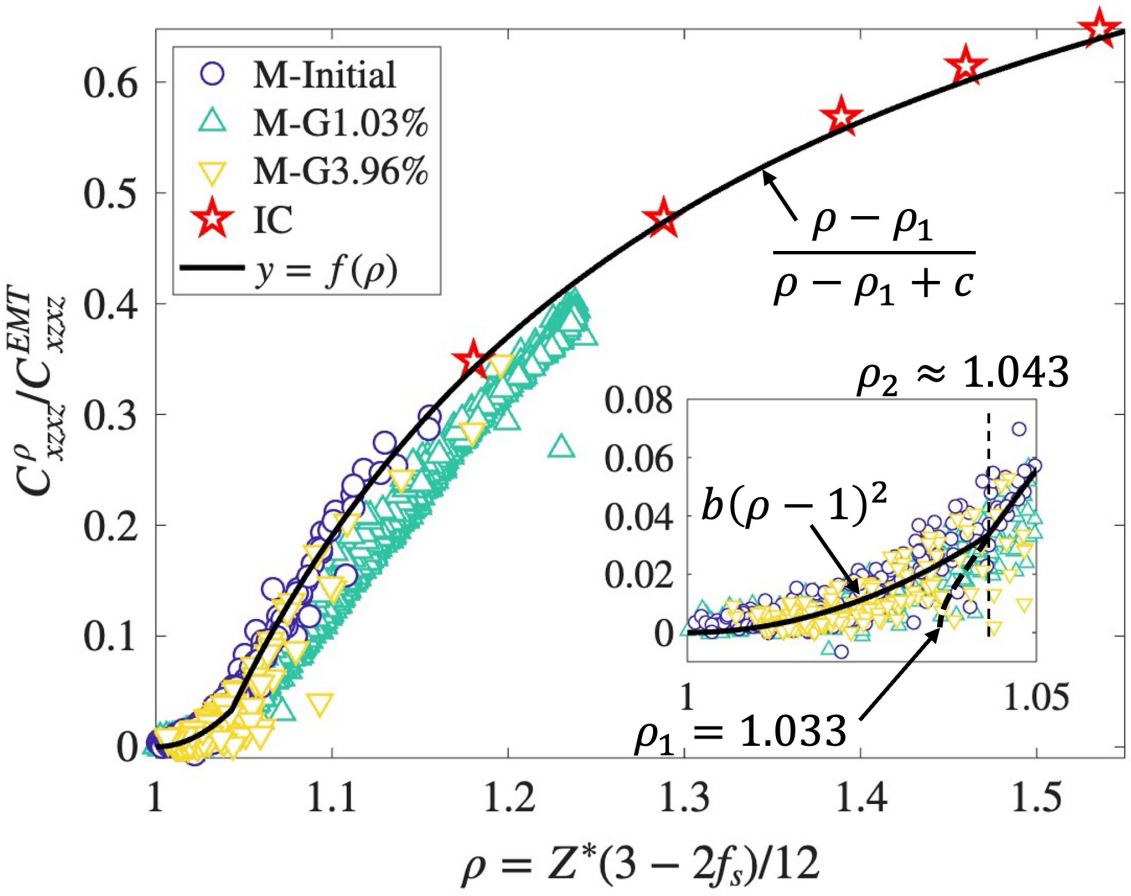


Figure 5: Normalised shear modulus $C^{\rho}_{xzxz}/C^{\mathrm{EMT}}_{xzxz}$ versus redundancy index ρ.

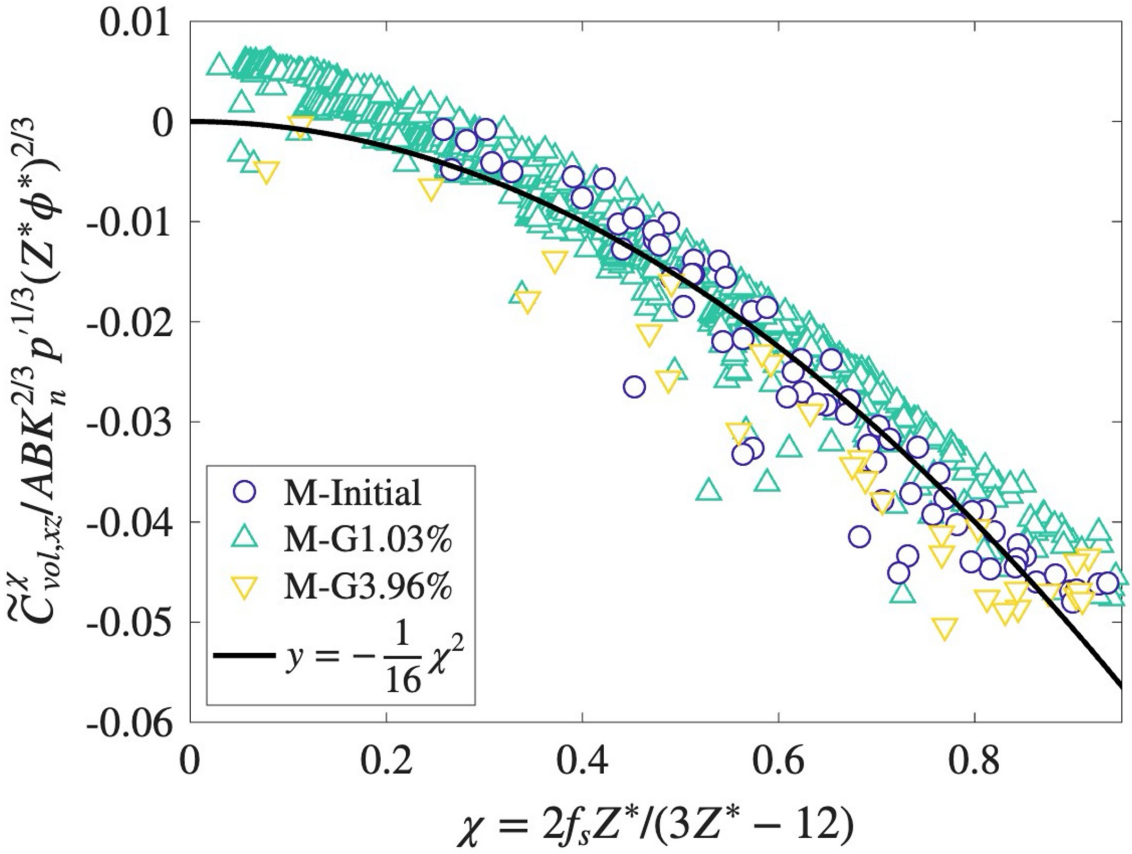


Figure 6: Normalised $\tilde{C}^{\chi}_{\mathrm{vol},xz}$ versus instability ratio χ.

When no contacts slide ($f_\mathrm{s} = 0$), $\mathrm{d}p'^{\mathrm{sliding}} = 0$, whereas an increasing fraction of sliding contacts is expected to amplify $|\mathrm{d}p'^{\mathrm{sliding}}|$. It is therefore convenient to introduce an internal variable that equals 0 at $f_\mathrm{s} = 0$ and reaches 1 at the mechanical stability limit ($\rho = 1$). Accordingly, we define the *instability ratio* χ—the ratio of constraints lost through contact sliding to the redundant constraints available without sliding—as

$$\chi \equiv \frac{2 f_\mathrm{s} Z^*}{3Z^* - 12} \leq 1. \tag{32}$$

Defining the sliding-induced volumetric–shear coupling modulus as

$$C^{\chi}_{\mathrm{vol},xz} \equiv \frac{3\,\mathrm{d}p'^{\mathrm{sliding}}}{\mathrm{d}\gamma_{xz}}, \tag{33}$$

and noting that $\mathrm{d}p'^{\mathrm{sliding}} < 0$ in almost all cases, we account for the loading direction via

$$\tilde{C}^{\chi}_{\mathrm{vol},xz} \equiv C^{\chi}_{\mathrm{vol},xz}\mathrm{sign}(\mathrm{d}\gamma_{xz}) = \frac{3\,\mathrm{d}p'^{\mathrm{sliding}}}{|\mathrm{d}\gamma_{xz}|}. \tag{34}$$

Figure 6 plots the normalised $\tilde{C}^{\chi}_{\mathrm{vol},xz}$ against χ for the M-Initial, M-G1.03%, and M-G3.96% samples. Although $\tilde{C}^{\chi}_{\mathrm{vol},xz} = 0$ is expected at $\chi = 0$, a few points take slightly positive values owing to minor closure errors in $C^{\alpha}_{\mathrm{vol},xz}$ (Figure 4). Nevertheless, all three samples share a clear common trend despite their contrasting liquefaction resistances: $\tilde{C}^{\chi}_{\mathrm{vol},xz}$ becomes increasingly negative with rising χ, confirming that contact sliding drives contraction. We capture this trend by

$$\tilde{C}^{\chi}_{\mathrm{vol},xz} = -a\chi^2 ABK_\mathrm{n}^{2/3} p'^{1/3} (Z^*\phi^*)^{2/3}, \tag{35}$$

where $a = 1/16$ is an empirical constant.

4.6 Resulting model expression

Combining the shear and volumetric components yields closed-form expressions for $\mathrm{d}\tau_{xz}$ and $\mathrm{d}p'$ during undrained cyclic simple shear in the xz-plane:

$$\mathrm{d}\tau_{xz}^{\mathrm{Model}} = f(\rho) B \frac{2A+3}{30} K_\mathrm{n}^{\frac{2}{3}} (Z^*\phi^*)^{\frac{2}{3}} p'^{\frac{1}{3}} \mathrm{d}\gamma_{xz} + \eta\,\mathrm{d}p'^{\mathrm{Model}}, \tag{36}$$

$$\mathrm{d}p'^{\mathrm{Model}} = \left(k_{\mathrm{vol}}\tilde{\alpha} - a\chi^2\right) \frac{|\mathrm{d}\gamma_{xz}|}{3} ABK_\mathrm{n}^{\frac{2}{3}} (Z^*\phi^*)^{\frac{2}{3}} p'^{\frac{1}{3}}. \tag{37}$$

The formulation comprises:

(i) three internal variables, ρ, $\tilde{\alpha} \equiv \alpha\,\mathrm{sign}(\mathrm{d}\gamma_{xz})$, and χ, derived analytically from measurable microscopic quantities Z^*, f_s, and f_{xz} (equations (28), (22), and (32));

(ii) the stress state variables p' and $\eta \equiv \tau_{xz}/p'$, which enter analytically via Hertzian contact stiffness and the SFF relationship rather than through empirical fitting;

(iii) the mechanical solid fraction ϕ^* (equation (8)), also incorporated analytically;

(iv) the material constants A, B, and K_n, determined analytically from the particle shear modulus and Poisson's ratio ($G_\mathrm{p}, \nu_\mathrm{p}$) (equations (13), (19), and (1)); and

(v) five empirical fitting constants: $a = \frac{1}{16}$, $b = \frac{1}{8}$, $c = 0.283$, $k_{\mathrm{vol}} = 1.5$, and $\rho_1 = 1.033$.

Each term in equations (36) and (37) has a distinct physical role, as follows:

(i) The ρ term represents the net shear stiffness attenuated by non-affine relaxation (Zaccone & Scossa-Romano, 2011): it approaches the affine EMT modulus as contact redundancy increases and vanishes at the mechanical stability limit ($\rho \to 1$).

(ii) The η term accounts for the shear stress change induced by variations in p' at a given stress ratio; as shown later, this contribution is minor compared with the ρ term except near the mechanical stability limit.

(iii) The $\tilde{\alpha}$ term governs anisotropy-induced dilatancy: when the stiffness-weighted anisotropy aligns with the loading direction ($\tilde{\alpha} > 0$), the sample dilates, whereas $\tilde{\alpha} < 0$ induces contraction.

(iv) The χ term captures sliding-induced contraction, which becomes increasingly negative as the instability ratio rises.

Dividing equation (36) by equation (37) yields the stress-path slope in p'–τ_{xz} space:

$$\frac{\mathrm{d}\tau_{xz}^{\mathrm{Model}}}{\mathrm{d}p'^{\mathrm{Model}}} = \frac{2A+3}{10A}\frac{f(\rho)\,\mathrm{sign}(\mathrm{d}\gamma_{xz})}{k_{\mathrm{vol}}\tilde{\alpha} - a\chi^2} + \eta, \tag{38}$$

in which K_{n}, $p'^{1/3}$, and $(Z^*\phi^*)^{2/3}$ cancel out completely, leaving only $A(\nu_{\mathrm{p}})$ and dimensionless state variables. Equation (38) directly reveals that phase transformation ($|\mathrm{d}\tau_{xz}/\mathrm{d}p'| \to \infty$, i.e. $\mathrm{d}p' = 0$) occurs when $k_{\mathrm{vol}}\tilde{\alpha} = a\chi^2$, whereas near the mechanical stability limit ($f(\rho) \to 0$), the slope approaches $\mathrm{d}\tau_{xz}/\mathrm{d}p' \approx \eta = \tau_{xz}/p'$.

5 Results

Equations (36) and (37) were validated against the main constant-volume cyclic shear simulations of all 24 M- and D-series samples in Table 1. Each loading cycle was divided into four segments: (i) $\tau_{xz} = 0 \to 15$ kPa, (ii) $\tau_{xz} = 15 \to 0$ kPa, (iii) $\tau_{xz} = 0 \to -15$ kPa, and (iv) $\tau_{xz} = -15 \to 0$ kPa. Four evaluation points were selected per segment; at each point, the instantaneous packing and fabric variables ($\phi^*, Z^*, f_{\mathrm{s}}, f_{xz}$) and stress state ($p', \tau_{xz}$) were substituted into equations (36) and (37), and the predicted increments $\mathrm{d}\tau_{xz}^{\mathrm{Model}}$ and $\mathrm{d}p'^{\mathrm{Model}}$ were compared with $\mathrm{d}\tau_{xz}^{\mathrm{DEM}}$ and $\mathrm{d}p'^{\mathrm{DEM}}$ over $|\mathrm{d}\gamma_{xz}| = 1.0 \times 10^{-5}$.

Figure 7 compares the predicted and DEM $(\mathrm{d}p', \mathrm{d}\tau_{xz})$ vectors along the stress path of M-Initial (showing two points per segment and magnifying vector lengths eightfold for clarity). Vectors along the failure envelope and near liquefaction remain barely visible owing to the small magnitudes of $\mathrm{d}p'$ and $\mathrm{d}\tau_{xz}$; this regime is examined separately in the next section. Overall, the model predictions agree closely with the DEM results across the entire stress path.

Figure 8 compares $\mathrm{d}p'^{\mathrm{Model}}$ against $\mathrm{d}p'^{\mathrm{DEM}}$ for (a) the 12 medium-dense samples and (b) the 12 dense samples, and $\mathrm{d}\tau_{xz}^{\mathrm{Model}}$ against $\mathrm{d}\tau_{xz}^{\mathrm{DEM}}$ in (c) and (d), respectively. Excellent agreement is achieved for both stress increments across all samples with diverse densities and liquefaction resistances, demonstrating that the proposed closed-form model reliably links the instantaneous micromechanical state to the macroscopic stress–dilatancy response.

6 Discussion

Because the developed model (equations (36) and (37)) accurately predicts $\mathrm{d}\tau_{xz}$ and $\mathrm{d}p'$ across a variety of samples and stress states, it can be used to interpret undrained cyclic stress paths from a micromechanical perspective. Here, we examine the characteristic stress-path features introduced in the Introduction and highlighted in Figure 1.

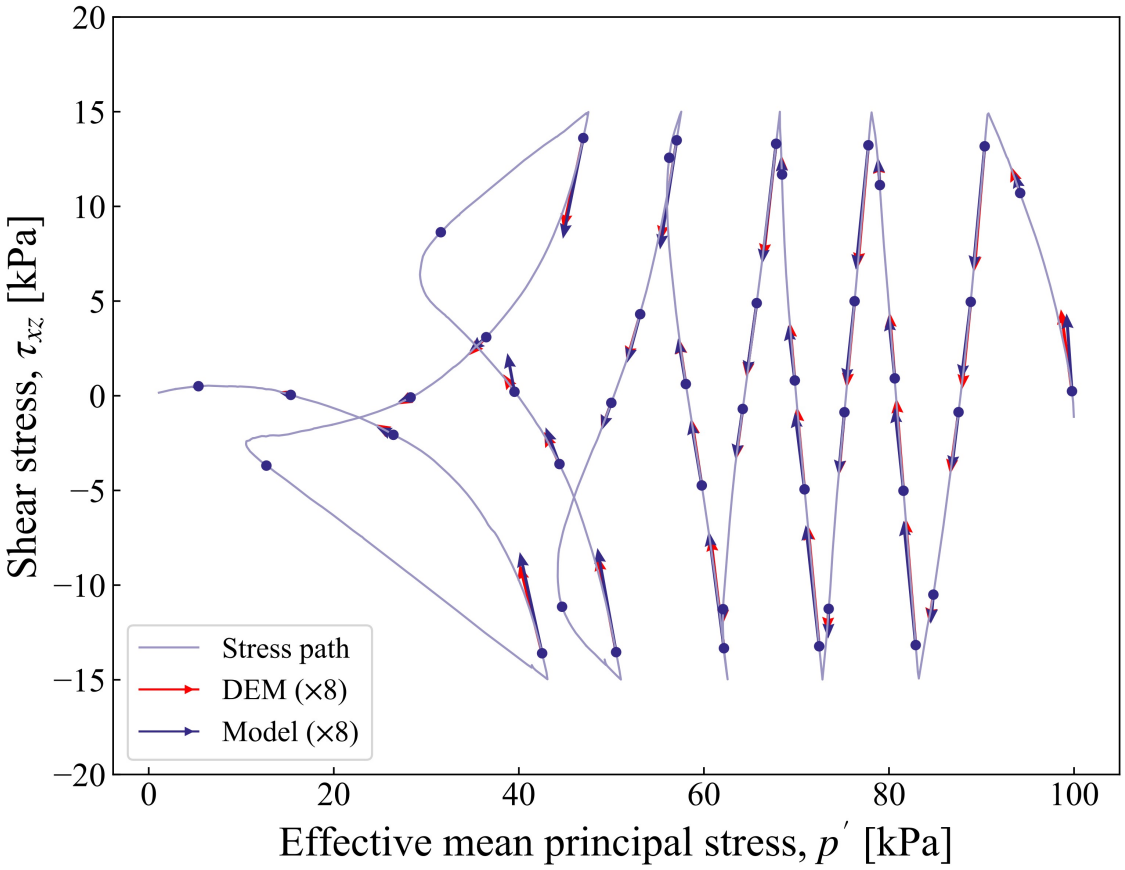


Figure 7: Comparison of model and DEM $(\mathrm{d}p', \mathrm{d}\tau_{xz})$ vectors at selected points along the stress path of M-Initial.

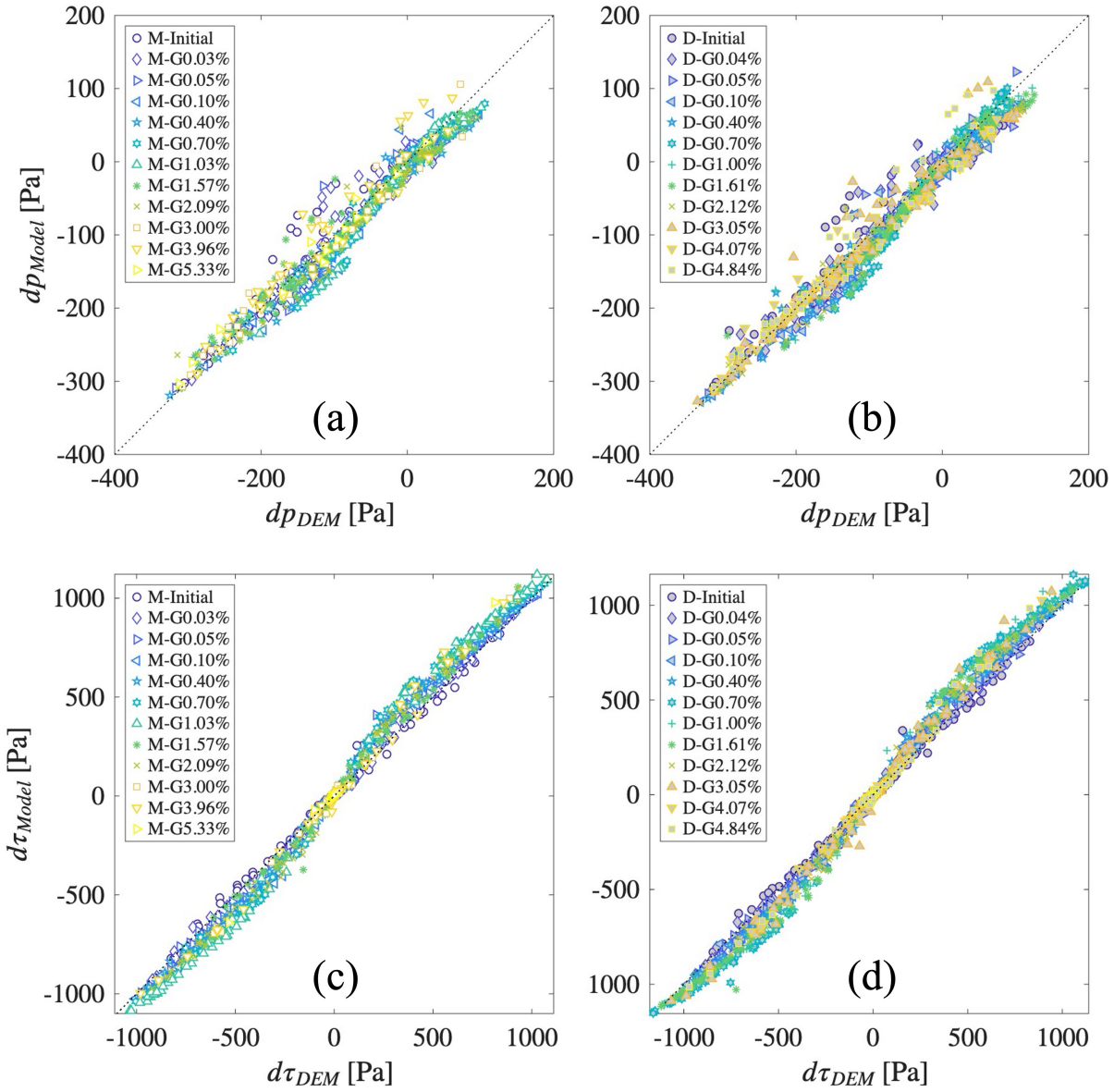


Figure 8: Comparison of model predictions and DEM results: (a) dp' for medium-dense (M) samples, (b) dp' for dense (D) samples, (c) dτ_{xz} for M samples, and (d) dτ_{xz} for D samples.

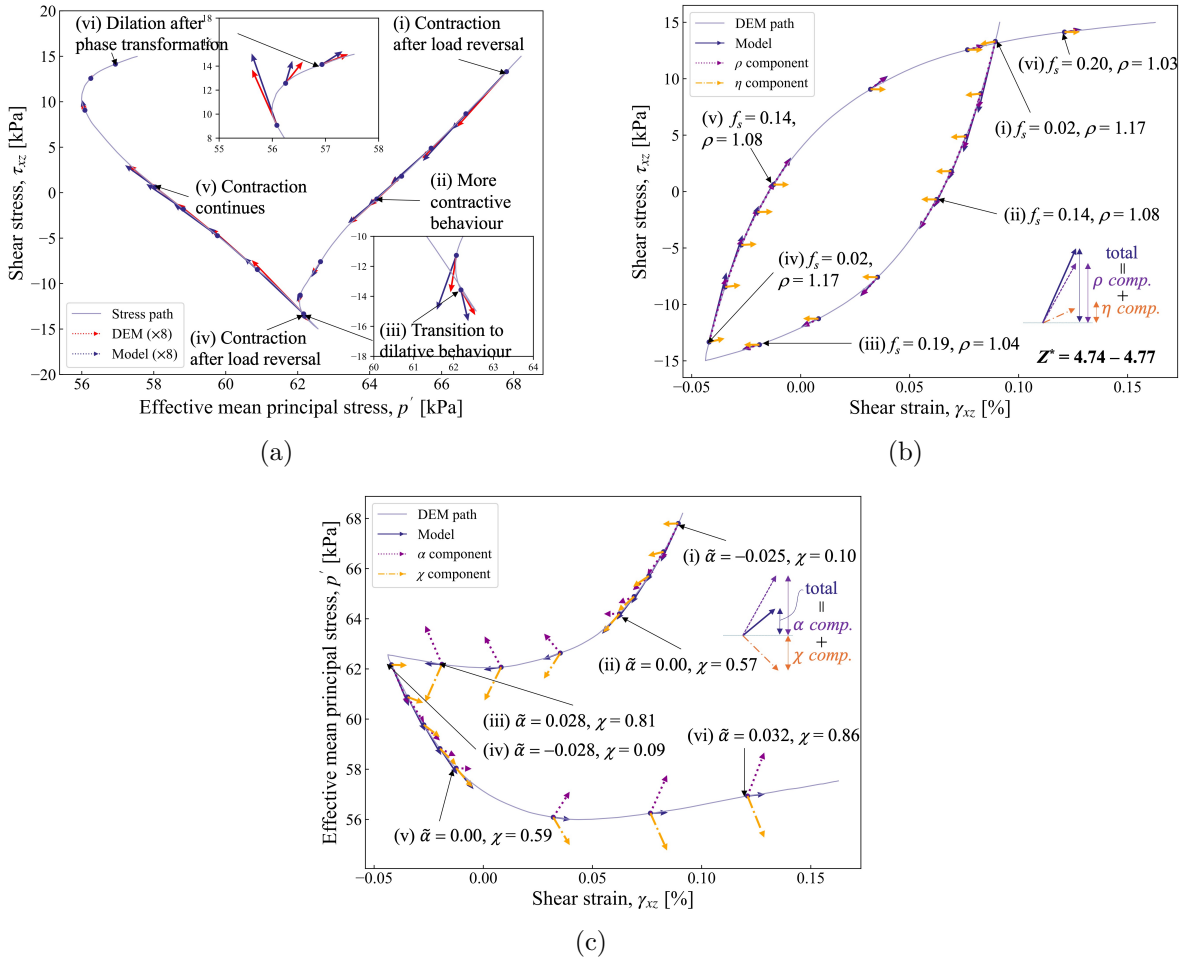


Figure 9: Behaviour of the M-Initial sample during cyclic simple shear across two load reversals: (a) stress path with $(\mathrm{d}p', \mathrm{d}\tau_{xz})$ vectors from the model and DEM (magnified eightfold), (b) stress–strain relationship with $(\mathrm{d}\gamma_{xz}, \mathrm{d}\tau_{xz}^{\mathrm{Model}})$ vectors decomposed into ρ and η components, and (c) p'–γ_{xz} relationship with $(\mathrm{d}\gamma_{xz}, \mathrm{d}p'^{\mathrm{Model}})$ vectors decomposed into α and χ components.

6.1 Load reversal and phase transformation

Figure 9(a) shows a segment of the M-Initial stress path spanning two load reversals (also highlighted in Figure 1(a)), which exhibits six key stages:

(i) contraction (a drop in p') immediately follows the first load reversal;

(ii) contraction becomes steeper in p'–τ_{xz} space, i.e. $\mathrm{d}p'/|\mathrm{d}\tau_{xz}|$ becomes more negative; and

(iii) the response transitions to dilation (an increase in p'), i.e. phase transformation.

Following the second load reversal:

(iv) the sample again exhibits contraction despite dilating immediately beforehand;

(v) contraction persists as shearing continues; and

(vi) dilation resumes after phase transformation, becoming more pronounced as cyclic shearing progresses.

Figures 9(b) and (c) plot the corresponding τ_{xz}–γ_{xz} and p'–γ_{xz} relationships, annotated with the relevant internal variables at points (i)–(vi). At point (i) just after the first load reversal, the sliding fraction f_s is close to zero, yielding a high redundancy index ρ and hence a high shear stiffness ($C_{xzxz} = \mathrm{d}\tau_{xz}/\mathrm{d}\gamma_{xz}$; Figure 9(b)). In the p'–γ_{xz} plot (Figure 9(c)), this low f_s gives a small instability ratio χ, so sliding-induced contraction is negligible at point (i); however, because $\mathrm{d}\gamma_{xz} < 0$ while $\tau_{xz}/p' > 0$ remains large, $\tilde{\alpha}$ is negative and drives substantial anisotropy-induced contraction.

As shearing proceeds from point (i) to (ii) (Figure 9(b)), f_s increases and ρ decreases, reducing the shear modulus. At point (ii) in Figure 9(c), where $\tau_{xz} \approx 0$ and hence $\tilde{\alpha} \approx 0$, the elevated χ resulting from increased contact sliding becomes the primary driver of contraction (further steepening $\mathrm{d}p'/|\mathrm{d}\tau_{xz}|$ together with the reduced shear stiffness).

Around point (iii) in Figure 9(c), $\tilde{\alpha}$ turns positive and produces a dilative α component in $\mathrm{d}p'$, whereas the χ component remains negative. These two competing mechanisms offset one another at phase transformation, beyond which the dilative α component outweighs the contractive χ component as $\tilde{\alpha}$ grows. This sequence of post-reversal contraction (point (iv)) and post-phase-transformation dilation (point (vi)) becomes increasingly prominent in later cycles as $|\tau_{xz}/p'|$, and hence $|\tilde{\alpha}|$, rises with decreasing p'.

6.2 Failure envelope and liquefaction

Figure 10(a) shows a segment of the M-Initial stress path approaching initial liquefaction ($p' < 1$ kPa). Because both the shear modulus and dilatancy increments become very small in this regime, the $(\mathrm{d}p', \mathrm{d}\tau_{xz})$ vectors are magnified 30-fold. As indicated in Figure 10(a):

(i) pronounced dilation occurs after phase transformation;

(ii) drastic contraction follows load reversal;

(iii) the dilative trajectory aligns closely with the failure envelope; and

(iv) the sample eventually reaches liquefaction.

As shown in the stress–strain curve in Figure 10(b), points (i)–(iv) all exhibit ρ values very close to unity ($\rho \leq 1.03$), meaning that the ρ component of $\mathrm{d}\tau_{xz}$ nearly vanishes (Figure 5). Consequently, $\mathrm{d}\tau_{xz}$ in equation (36) is driven predominantly by $\eta\,\mathrm{d}p'$.

Meanwhile, the p'–γ_{xz} relationship in Figure 10(c) indicates that χ approaches unity at points (i)–(iv) owing to high f_s, producing a strongly negative (contractive) χ component; hence,

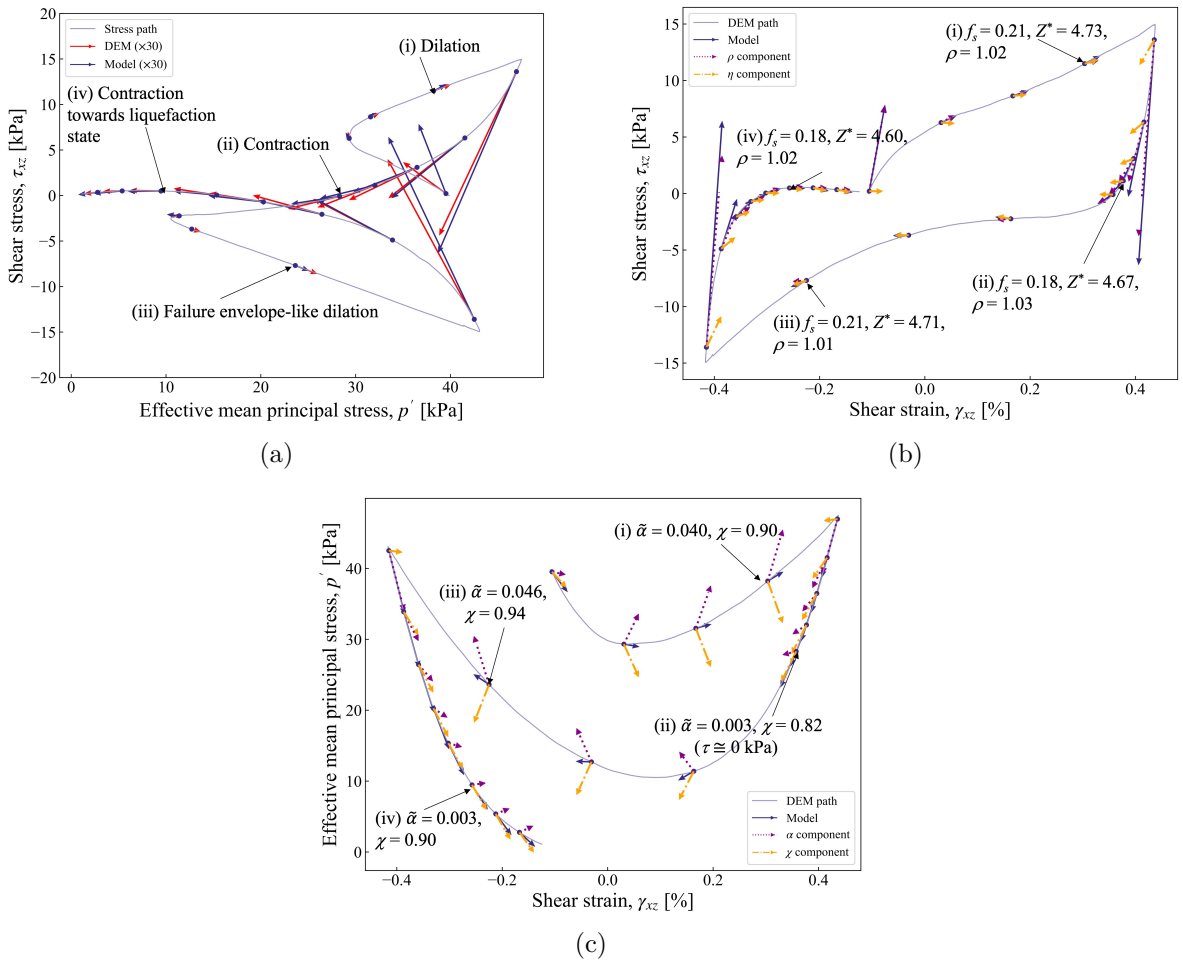


Figure 10: Behaviour of the M-Initial sample during cyclic simple shear near liquefaction: (a) stress path with $(\mathrm{d}p', \mathrm{d}\tau_{xz})$ vectors from the model and DEM (magnified 30-fold), (b) stress–strain relationship, and (c) p'–γ_{xz} relationship (vector notation as in Figure 9).

the sample undergoes drastic contraction unless $\tilde{\alpha}$ is sufficiently large. Specifically, low $\tilde{\alpha}$ values at points (ii) and (iv) result in rapid contraction, whereas high $\tilde{\alpha}$ values at points (i) and (iii) produce net dilation.

Within the present framework, therefore, motion along the failure envelope and approach to liquefaction both emerge as $\rho \to 1$ ($C^{\rho}_{xzxz} \to 0$), distinguished by the sign of $\mathrm{d}p'$: at high stress ratios $|\tau_{xz}/p'|$, strong anisotropy ($\tilde{\alpha} > 0$) drives dilation ($\mathrm{d}p' > 0$) while maintaining an approximately constant τ_{xz}/p', whereas at low stress ratios after load reversal, extensive contact sliding drives contraction ($\mathrm{d}p' < 0$) towards $p' = 0$. Nevertheless, because contact-network rearrangements and stick–slip transitions occur frequently near the mechanical stability limit ($\rho \to 1$), more rigorous particle-scale investigation of this regime is left for future work.

6.3 Shear history effect

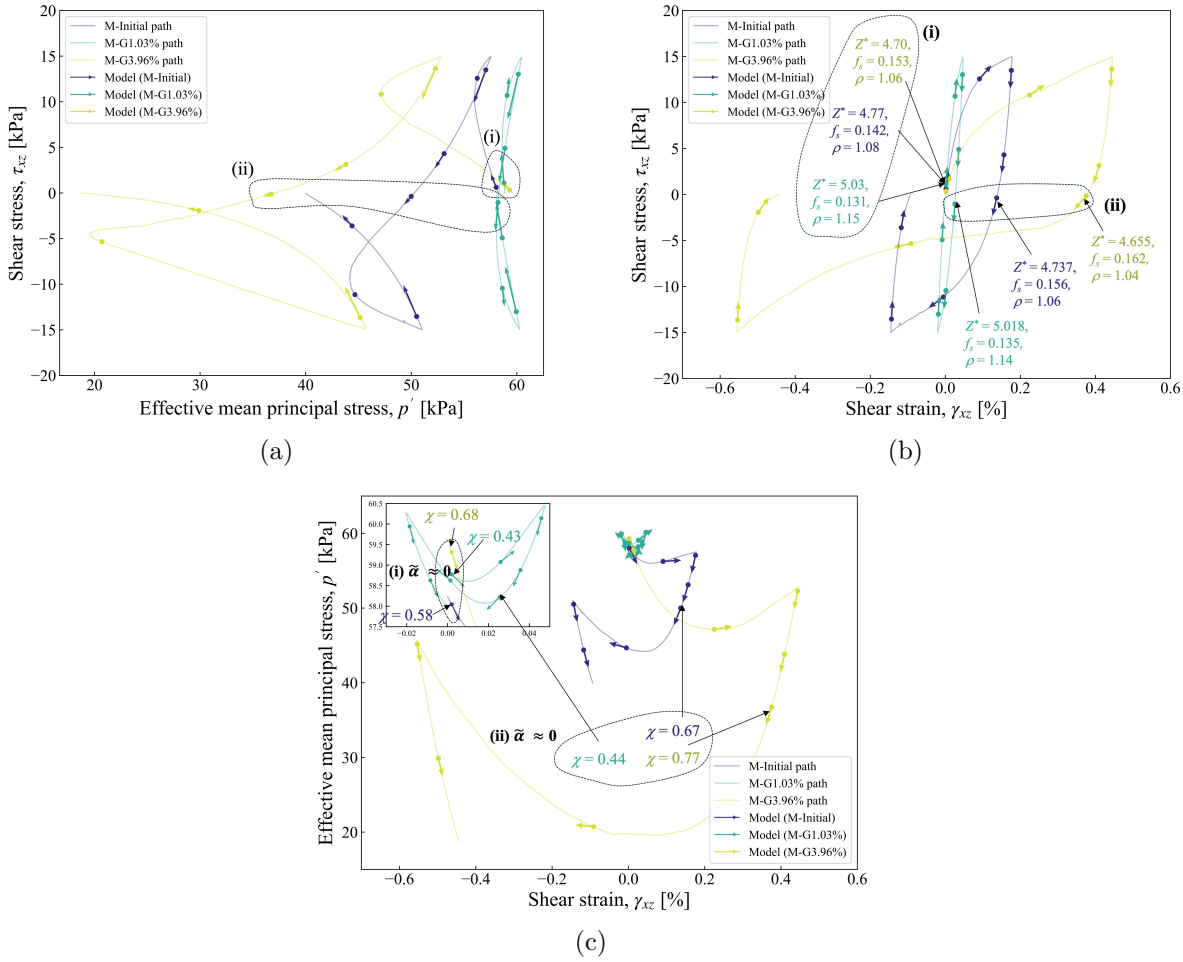


Figure 11: Comparison of M-Initial, M-G1.03%, and M-G3.96% over a shear cycle starting from $p' \approx 60$ kPa and $\tau_{xz} \approx 0$ kPa: (a) stress paths with $(\mathrm{d}p', \mathrm{d}\tau_{xz})$ vectors from the model and DEM (magnified eightfold), (b) stress–strain relationships, and (c) p'–γ_{xz} relationships.

A primary motivation of this study is to explain the cyclic shear history effect in sand: small cyclic pre-shearing renders sand stiffer and less contractive (M-G1.03% in Figure 1(b)), whereas large pre-shearing makes it softer and highly contractive (M-G3.96% in Figure 1(c)). Figure 11(a) compares one loading cycle starting from $\tau_{xz} \approx 0$ kPa and $p' \approx 60$ kPa for M-Initial, M-G1.03%, and M-G3.96%. Despite having nearly identical densities and starting stress states, the three samples trace markedly different trajectories, whose $(\mathrm{d}p', \mathrm{d}\tau_{xz})$ responses are well captured by the proposed model (Figure 11(a)).

Regions (i) and (ii) in Figure 11(a) compare the three samples near $\tau_{xz} \approx 0$ kPa, where M-G1.03% is stiffer and less contractive while M-G3.96% is softer and more contractive. As indicated in Figures 11(b) and (c), M-G1.03% maintains a higher Z^* and a lower f_s, yielding both a higher redundancy index ρ (greater stiffness) and a lower instability ratio χ (reduced contraction). Conversely, M-G3.96% exhibits a lower Z^* combined with a higher f_s, driving both ρ and χ close to unity and producing soft, strongly contractive behaviour.

6.4 Anisotropy and flow-like contraction

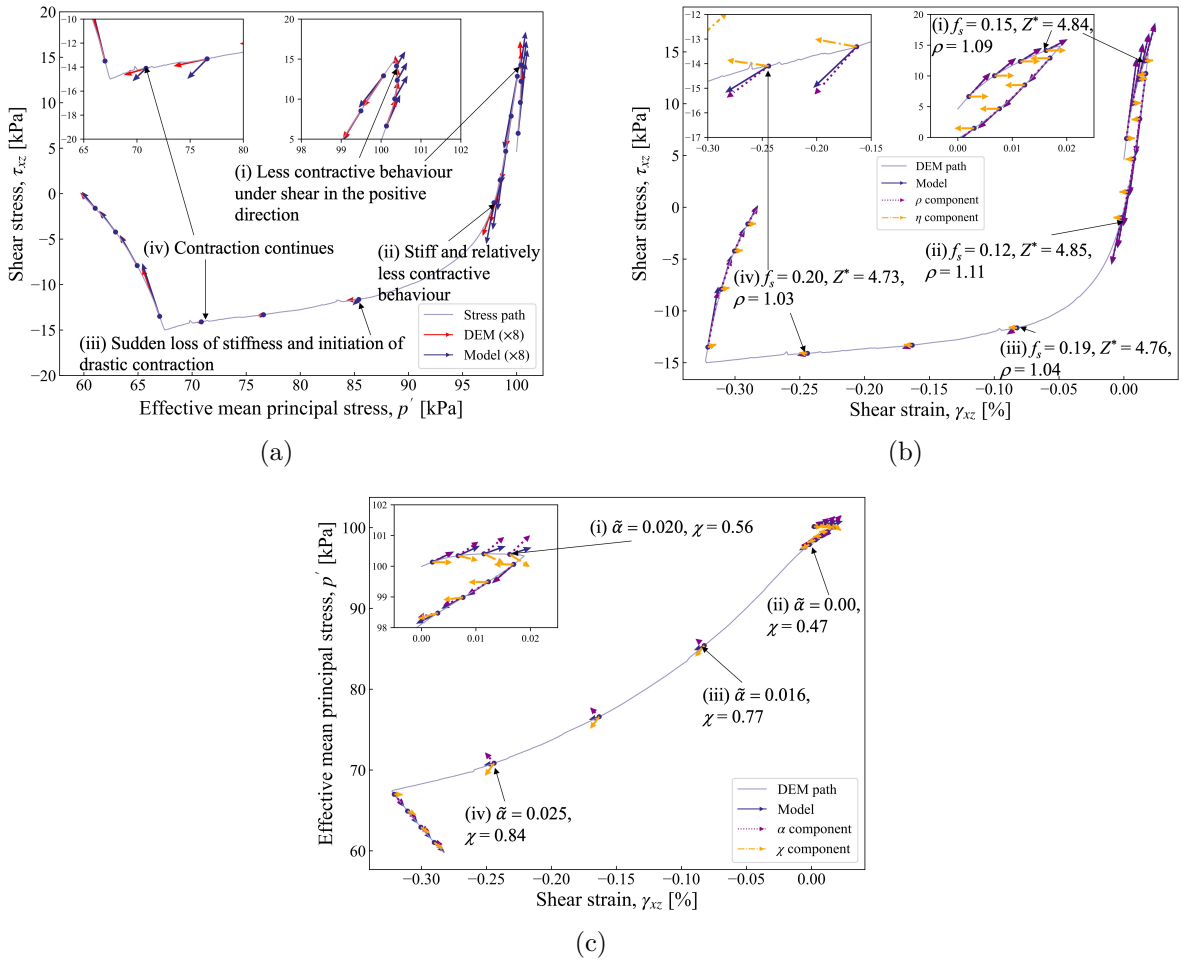


Figure 12: Behaviour of the M-G3.96% sample during the first shear cycle: (a) stress path with $(\mathrm{d}p', \mathrm{d}\tau_{xz})$ vectors from the model and DEM (magnified eightfold), (b) stress–strain relationship, and (c) p'–γ_{xz} relationship (vector notation as in Figure 9).

Figure 12(a) shows the first-cycle stress path of M-G3.96%, which displays pronounced anisotropic behaviour:

(i) the sample is stiff and dilative under positive shear ($\mathrm{d}\gamma_{xz} > 0$);

(ii) stiff, weakly contractive behaviour briefly continues immediately after load reversal;

(iii) rapid stiffness degradation and drastic contraction initiate during negative shear ($\mathrm{d}\gamma_{xz} < 0$); and

(iv) $\mathrm{d}\tau_{xz}$ approaches zero while contraction persists ($\mathrm{d}p' < 0$), producing flow-like contraction and a severe loss of effective stress within the first cycle.

Figures 12(b) and (c) show the corresponding τ_{xz}–γ_{xz} and p'–γ_{xz} responses. At point (i), $\rho \approx 1.1$ provides relatively high shear stiffness, while M-G3.96% simultaneously possesses a notably positive $\tilde{\alpha}$ (Figure 12(c)) inherited from its initial fabric anisotropy ($f_{xz} > 0$; Table 1), resulting in dilation. Between points (ii) and (iii) (Figure 12(b)), Z^* drops from 4.85 to 4.76 while f_s rises, causing a sharp decrease in ρ and increase in χ. By point (iv), both ρ and χ approach unity, meaning that shear stiffness nearly vanishes ($\rho \to 1$) while sliding-induced contraction persists ($\chi \to 1$).

Although the model qualitatively captures this transition from stiff, dilative behaviour to soft, contractive behaviour, achieving close quantitative agreement during the flow-like stage between points (iii) and (iv) remains challenging (Figure 12(a)). Along this segment, $\mathrm{d}\tau_{xz}^{\mathrm{DEM}}$ becomes very small and the C_{xzxz}^{ρ}–ρ data in Figure 5 exhibit greater relative scatter as $\rho \to 1$. Simultaneously, the α and χ components take opposite signs with comparable magnitudes (Figure 12(c)); because $\mathrm{d}p'^{\mathrm{Model}}$ is their algebraic sum, minor scatter in the $C_{\mathrm{vol},xz}^{\alpha}$–$\alpha$ and $\tilde{C}_{\mathrm{vol},xz}^{\chi}$–$\chi$ relations (Figures 4 and 6) becomes non-negligible. Consequently, the stress-path tangent vector $(\mathrm{d}p', \mathrm{d}\tau_{xz})$ is particularly sensitive to small prediction errors when both $\mathrm{d}p' \approx 0$ and $\mathrm{d}\tau_{xz} \approx 0$, as occurs during this flow-like contraction.

7 Conclusions

This study proposed closed-form micromechanical expressions for the shear modulus and volumetric–shear coupling modulus to predict increments in shear stress ($\mathrm{d}\tau_{xz}$) and effective mean principal stress ($\mathrm{d}p'$) during undrained cyclic simple shear. Building on Effective Medium Theory (EMT) (Walton, 1987; Chang et al., 1989), which analytically links grain-scale material properties to macroscopic moduli, we incorporated the effects of non-affine relaxation and contact sliding for sphere packings with finite inter-particle friction, extending analytical results for frictionless spheres (Lemaître & Maloney, 2006; Zaccone & Scossa-Romano, 2011) and semi-analytical results in the non-sliding regime (Morimoto, 2027).

Using constant-volume cyclic simple shear DEM simulations, $\mathrm{d}\tau_{xz}$ and $\mathrm{d}p'$ were formulated in equations (36) and (37) in terms of three derived internal variables:

(i) the redundancy index (ρ), the ratio of total contact constraints to particle degrees of freedom (Kruyt & Rothenburg, 2009; Kruyt, 2010; Gong et al., 2012);

(ii) the instability ratio (χ), the ratio of constraints lost through contact sliding to the redundant constraints available without sliding; and

(iii) the stiffness-weighted contact normal anisotropy (α) (Morimoto, 2027).

A decrease in ρ degrades the shear modulus, an increase in χ drives sliding-induced contraction, and $\tilde{\alpha} \equiv \alpha\,\mathrm{sign}(\mathrm{d}\gamma_{xz})$ induces dilation for $\tilde{\alpha} > 0$ or contraction for $\tilde{\alpha} < 0$. Crucially, all three internal variables are derived analytically from standard, directly measurable DEM quantities: the mechanical coordination number (Z^*), sliding contact fraction (f_s), and contact normal fabric anisotropy (f_{xz}). Model predictions agree closely with DEM results at arbitrary points along cyclic stress paths across samples spanning a wide range of densities and pre-shear histories.

The model provides a clear micromechanical interpretation of undrained cyclic stress paths. Phase transformation (Ishihara et al., 1975), the transition from contraction to dilation, occurs when anisotropy-induced dilation ($\tilde{\alpha} > 0$) overcomes sliding-induced contraction (χ). Furthermore, the contrasting effects of pre-shear history, whereby small cyclic pre-shearing produces stiff, weakly contractive behaviour while large pre-shearing leads to soft, strongly contractive behaviour, are explicitly explained by differences in Z^* and f_s (and hence ρ and χ).

Because the present formulation assumes nearly monodisperse spheres at a fixed inter-particle friction coefficient, generalisation to polydisperse, non-spherical grains and varied friction coefficients is needed for quantitative application to natural sands. Formulating evolution laws for

Z^*, f_s, and f_{xz} is also required to integrate full stress paths as in continuum constitutive models; given that these three variables are readily measurable in DEM, developing such evolution laws represents a promising avenue for future work.

8 Acknowledgements

This work was supported by JSPS KAKENHI Grant Numbers 23K19137 and 26K01039. This research was conducted using the FUJITSU Supercomputer PRIMEHPC FX1000 and FUJITSU Server PRIMERGY GX2570 (Wisteria/BDEC-01) at the Information Technology Center, The University of Tokyo.

9 Notation

A	contact stiffness ratio (equation (13))
a	empirical fitting constant for $C^{\chi}_{\mathrm{vol},xz}$
B	material constant (equation (19))
b	empirical fitting constant for C^{ρ}_{xzxz}
C^{EMT}	modulus estimated by Effective Medium Theory
C_{xzxz}	shear modulus
C^{ρ}_{xzxz}	shear modulus related to redundancy
$C_{\mathrm{vol},xz}$	volumetric–shear coupling modulus
$C^{\alpha}_{\mathrm{vol},xz}$	volumetric–shear coupling modulus related to anisotropy
$C^{\chi}_{\mathrm{vol},xz}$	volumetric–shear coupling modulus related to contact sliding
c	empirical fitting constant for C^{ρ}_{xzxz}
D_{50}	median particle diameter
e	void ratio
$\mathbf{F}_\mathrm{n}, \mathbf{F}_\mathrm{t}$	contact normal and tangential force vectors
F_n	contact normal force magnitude
f_{ij}	deviatoric contact-normal fabric tensor
f_s	sliding fraction
G_p	shear modulus of particles
I	inertial number
K_n, K_t	normal and tangential contact stiffness parameters
k_n, k_t	incremental normal and tangential contact stiffnesses
k_vol	empirical fitting constant for $C^{\alpha}_{\mathrm{vol},xz}$
L	distance between centres of contacting particles
N_c, N^*_c	numbers of contacts and mechanical contacts
$N^{*\mathrm{stick}}_\mathrm{c}$	number of sticking mechanical contacts
$N^{*\mathrm{sliding}}_\mathrm{c}$	numbers of sliding mechanical contacts
N_L	number of cycles to initial liquefaction
N_p, N^*_p	numbers of particles and non-rattler particles
$\mathbf{n}$	contact normal unit vector
p'	effective mean principal stress
R, R^*	radius and equivalent radius
$\Delta\mathbf{s}_\mathrm{t}$	tangential displacement vector
V, V^*_s	volumes of granular system and non-rattler particles
Z, Z^*, Z^*_crit	coordination number, mechanical coordination number, critical mechanical coordination number

α	stiffness-weighted contact normal fabric anisotropy (equation (22))
χ	instability ratio (equation (32))
δ	contact overlap
δ_{ij}	Kronecker delta
η	stress ratio (τ_{xz}/p')
γ_{DAmax}	maximum double-amplitude shear strain during pre-shear
γ_{xz}	shear strain
λ	empirical constant for non-sliding shear modulus (Morimoto, 2027)
μ	friction coefficient
ν_{p}	Poisson's ratio of particles
ϕ^*	mechanical solid fraction
ϕ_{ij}	second-order fabric tensor
ρ	redundancy index (equation (28))
ρ_1, ρ_2	empirical threshold and transition value for $f(\rho)$
ρ_{p}	density of particles
σ'_{ij}	effective stress tensor
τ_{xz}	shear stress
$\langle\cdot\rangle$	arithmetic mean over mechanical contacts
$\tilde{x}$	loading direction operator ($= x\mathrm{sign}(\mathrm{d}\gamma_{xz})$)

References

Arthur, J. R. F. & Menzies, B. K. (1972). Inherent anisotropy in a sand. *Géotechnique* **22**(1), 115–128.

Bathurst, R. J. & Rothenburg, L. (1990). Observations on stress–force–fabric relationships in idealized granular materials. *Mechanics of Materials* **9**(1), 65–80.

Been, K. & Jefferies, M. G. (1985). A state parameter for sands. *Géotechnique* **35**(2), 99–112.

Bolton, M. D. (1986). The strength and dilatancy of sands. *Géotechnique* **36**(1), 65–78.

Cavarretta, I. (2009). *The influence of particle characteristics on the engineering behaviour of granular materials*. PhD thesis, Imperial College London (University of London).

Chang, C. S., Sundaram, S. S. & Misra, A. (1989). Initial moduli of particulated mass with frictional contacts. *International Journal for Numerical and Analytical Methods in Geomechanics* **13**(6), 629–644.

Cundall, P. A. & Strack, O. D. L. (1979). A discrete numerical model for granular assemblies. *Géotechnique* **29**(1), 47–65.

Da Cruz, F., Emam, S., Prochnow, M., Roux, J. N. & Chevoir, F. (2005). Rheophysics of dense granular materials: discrete simulation of plane shear flows. *Physical Review E* **72**(2), 021309.

Dafalias, Y. F. & Manzari, M. T. (2004). Simple plasticity sand model accounting for fabric change effects. *Journal of Engineering Mechanics* **130**(6), 622–634.

De Silva, L. I. N., Koseki, J., Chiaro, G. & Sato, T. (2015). A stress–strain description of saturated sand under undrained cyclic torsional shear loading. *Soils and Foundations* **55**(3), 559–574.

Finn, W. D. L., Bransby, P. L. & Pickering, D. J. (1970). Effect of strain history on liquefaction of sand. *Journal of the Soil Mechanics and Foundations Division* **96**(SM6), 1917–1934.

Goddard, J. D. (1990). Nonlinear elasticity and pressure-dependent wave speeds in granular media. *Proceedings of the Royal Society of London. Series A, Mathematical and Physical Sciences* **430**, 105–131.

Gong, G., Thornton, C. & Chan, A. H. (2012). DEM simulations of undrained triaxial behavior of granular material. *Journal of Engineering Mechanics* **138**(6), 560–566.

Hardin, B. O. & Richart, F. E. Jr. (1963). Elastic wave velocities in granular soils. *Journal of the Soil Mechanics and Foundations Division* **89**(1), 33–65.

Hertz, H. R. (1882). Über die Berührung fester elastischer Körper und über die Härte. In *Verhandlungen des Vereins zur Beförderung des Gewerbefleisses*, Verein zur Beförderung des Gewerbefleisses, Berlin, pp. 449–463 (in German).

Hu, Q., Zhang, J.-M. & Wang, R. (2020). Quantification of dilatancy during undrained cyclic loading and liquefaction. *Computers and Geotechnics* **128**, 103853.

Ishihara, K., Tatsuoka, F. & Yasuda, S. (1975). Undrained deformation and liquefaction of sand under cyclic stresses. *Soils and Foundations* **15**(1), 29–44.

Ishihara, K. (1993). Liquefaction and flow failure during earthquakes. *Géotechnique* **43**(3), 351–451.

Ishihara, K. & Okada, S. (1978). Effects of stress history on cyclic behavior of sand. *Soils and Foundations* **18**(4), 31–45.

Ishihara, K. & Okada, S. (1982). Effects of large preshearing on cyclic behavior of sand. *Soils and Foundations* **22**(3), 109–125.

Kruyt, N. P. & Rothenburg, L. (2009). Plasticity of granular materials: a structural-mechanics view. In *AIP Conference Proceedings*, Vol. 1145, No. 1, pp. 1073–1076. American Institute of Physics.

Kruyt, N. P. (2010). Micromechanical study of plasticity of granular materials. *Comptes Rendus Mécanique* **338**(10–11), 596–603.

La Ragione, L. & Magnanimo, V. (2012). Evolution of the effective moduli of an anisotropic, dense, granular material. *Granular Matter* **14**(6), 749–757.

Lemaître, A. & Maloney, C. E. (2006). Sum rules for the quasi-static and visco-elastic response of disordered solids at zero temperature. *Journal of Statistical Physics* **123**(3), 415–453.

Li, X. S. & Dafalias, Y. F. (2012). Anisotropic critical state theory: role of fabric. *Journal of Engineering Mechanics* **138**(3), 263–275.

Magnanimo, V., La Ragione, L., Jenkins, J. T., Wang, P. & Makse, H. A. (2008). Characterizing the shear and bulk moduli of an idealized granular material. *Europhysics Letters* **81**(3), 34006.

Makse, H. A., Gland, N., Johnson, D. L. & Schwartz, L. M. (1999). Why effective medium theory fails in granular materials. *Physical Review Letters* **83**(24), 5070.

Mindlin, R. D. (1949). Compliance of elastic bodies in contact. *Journal of Applied Mechanics* **16**(3), 259–268.

Mindlin, R. D. & Deresiewicz, H. (1953). Elastic spheres in contact under varying oblique forces. *Journal of Applied Mechanics* **20**(3), 327–344.

Miura, S. & Toki, S. (1982). A sample preparation method and its effect on static and cyclic deformation-strength properties of sand. *Soils and Foundations* **22**(1), 61–77.

Monkul, M. M., Gültekin, C., Gülver, M., Akın, Ö. & Eseller-Bayat, E. (2015). Estimation of liquefaction potential from dry and saturated sandy soils under drained constant volume cyclic simple shear loading. *Soil Dynamics and Earthquake Engineering* **75**, 27–36.

Morimoto, T., Aoyagi, Y. & Koseki, J. (2019). Effects of induced anisotropy on multiple liquefaction properties of sand with initial static shear. *Soils and Foundations* **59**(5), 1148–1159.

Morimoto, T., Otsubo, M. & Koseki, J. (2021). Microscopic investigation into liquefaction resistance of pre-sheared sand: effects of particle shape and initial anisotropy. *Soils and Foundations* **61**(2), 335–351.

Morimoto, T. & Salomon, J. (2026). A unified approach to predicting re-liquefaction resistance of gap-graded soils. *Computers and Geotechnics* **190**, 107740.

Morimoto, T. (2027). A semi-analytical effective-medium model of small-strain stress-dilatancy during cyclic undrained shear: mechanical links to coordination number and contact fabric. *Computers and Geotechnics* **203**, 108763.

Oda, M. (1972). Initial fabrics and their relations to mechanical properties of granular material. *Soils and Foundations* **12**(1), 17–36.

Oda, M. (1982). Fabric tensor for discontinuous geological materials. *Soils and Foundations* **22**(4), 96–108.

Oda, M., Kawamoto, K., Suzuki, K., Fujimori, H. & Sato, M. (2001). Microstructural interpretation on reliquefaction of saturated granular soils under cyclic loading. *Journal of Geotechnical and Geoenvironmental Engineering* **127**(5), 416–423.

Ouadfel, H. & Rothenburg, L. (2001). 'Stress–force–fabric' relationship for assemblies of ellipsoids. *Mechanics of Materials* **33**(4), 201–221.

Papadimitriou, A. G. & Bouckovalas, G. D. (2002). Plasticity model for sand under small and large cyclic strains: a multiaxial formulation. *Soil Dynamics and Earthquake Engineering* **22**(3), 191–204.

Plimpton, S. (1995). Fast parallel algorithms for short-range molecular dynamics. *Journal of Computational Physics* **117**(1), 1–19.

Rothenburg, L. & Bathurst, R. J. (1989). Analytical study of induced anisotropy in idealized granular materials. *Géotechnique* **39**(4), 601–614.

Rowe, P. W. (1962). The stress–dilatancy relation for static equilibrium of an assembly of particles in contact. *Proceedings of the Royal Society of London. Series A, Mathematical and Physical Sciences* **269**, 500–527.

Satake, M. (1978). Constitution of mechanics of granular materials through the graph theory. In *Proceedings of the US–Japan Seminar on Continuum Mechanical and Statistical Approaches in the Mechanics of Granular Materials*, Sendai, Japan, pp. 203–215.

Senetakis, K., Coop, M. R. & Todisco, M. C. (2013). The inter-particle coefficient of friction at the contacts of Leighton Buzzard sand quartz minerals. *Soils and Foundations* **53**(5), 746–755.

Suzuki, T. & Suzuki, T. (1988). Effects of density and fabric change on reliquefaction resistance of saturated sand. *Journal of the Japanese Society of Soil Mechanics and Foundation Engineering* **28**(2), 187–195 (in Japanese).

Tatsuoka, F., Ochi, K., Fujii, S. & Okamoto, M. (1986). Cyclic undrained triaxial and torsional shear strength of sands for different sample preparation methods. *Soils and Foundations* **26**(3), 23–41.

Thompson, A. P. et al. (2022). LAMMPS—a flexible simulation tool for particle-based materials modeling at the atomic, meso, and continuum scales. *Computer Physics Communications* **271**, 108171.

Thornton, C. (2000). Numerical simulations of deviatoric shear deformation of granular media. *Géotechnique* **50**(1), 43–53.

Tsuji, Y., Tanaka, T. & Ishida, T. (1992). Lagrangian numerical simulation of plug flow of cohesionless particles in a horizontal pipe. *Powder Technology* **71**(3), 239–250.

Wahyudi, S., Koseki, J., Sato, T. & Chiaro, G. (2016). Multiple-liquefaction behavior of sand in cyclic simple stacked-ring shear tests. *International Journal of Geomechanics* **16**(5), C4015001.

Walton, K. (1987). The effective elastic moduli of a random packing of spheres. *Journal of the Mechanics and Physics of Solids* **35**(2), 213–226.

Wang, R., Fu, P., Zhang, J.-M. & Dafalias, Y. F. (2016). DEM study of fabric features governing undrained post-liquefaction shear deformation of sand. *Acta Geotechnica* **11**(6), 1321–1337.

Wang, R., Fu, P., Zhang, J.-M. & Dafalias, Y. F. (2019). Fabric characteristics and processes influencing the liquefaction and re-liquefaction of sand. *Soil Dynamics and Earthquake Engineering* **125**, 105720.

Wei, J. & Wang, G. (2017). Discrete-element method analysis of initial fabric effects on pre- and post-liquefaction behavior of sands. *Géotechnique Letters* **7**(2), 161–166.

Yamada, S., Takamori, T. & Sato, K. (2010). Effects on reliquefaction resistance produced by changes in anisotropy during liquefaction. *Soils and Foundations* **50**(1), 9–25.

Yang, S., Huang, D., Wang, G. & Jin, F. (2022). Probing fabric evolution and reliquefaction resistance of sands using discrete-element modeling. *Journal of Engineering Mechanics* **148**(6), 04022023.

Yimsiri, S. & Soga, K. (2000). Micromechanics-based stress–strain behaviour of soils at small strains. *Géotechnique* **50**(5), 559–571.

Yimsiri, S. & Soga, K. (2010). DEM analysis of soil fabric effects on behaviour of sand. *Géotechnique* **60**(6), 483–495.

Zaccone, A. & Scossa-Romano, G. (2011). Approximate analytical description of the nonaffine response of amorphous solids. *Physical Review B* **83**(18), 184205.

Zeng, S., Taiebat, M. & Dafalias, Y. F. (2026). SANISAND-FM: a sand plasticity model with fabric anisotropy and memory surface with emphasis on cyclic liquefaction. *Géotechnique* **76**(6), 787–804.